Chapter 1

Introduction

This chapter presents an introduction to information optics and delivering coherent optical signals through the free space and scattering media. The role of helical beams and holography in the delivery and recovery of optical information is discussed. This chapter also covers the challenges of faithful delivery of optical signals through randomness light, different techniques, limitations, and the role of coherence optics in optics through randomness particularly on looking through randomness.

1.1 Optical information processing

Optics is the branch of physics dealing with the phenomenon involving light. Light refers to electromagnetic radiation of frequencies within the visible range of 400-700 nm (Hecht, 2012). The term optical information can mean two things: the detection of the signal, and/or processing and use of the optical signal. The time or space-dependent information carried by the light signal is referred to as optical information. The amplitude or intensity, wavelength, polarization, and coherence are some fundamental properties of light that carry signatures of the optical signal (Goodman, 1968). For instance, an intensity image recorded by a camera at the end of the telescope which is coming from outer space, an intensity image captured by the endoscopy in medical imaging, a phase profile in the digital holographic microscope, and a polarization map in the polarimeter carry a significant amount of information in one dimensional (1D), two dimensional (2D) and three dimensional (3D) space. Depending on the nature of the detection, the use of optical signals can be broadly categorized in terms of qualitative and quantitative analysis. The human eye is a simple example of qualitative detection of optical information. On the other hand, sensors such as charged coupled devices (CCD)/CMOS can be used for quantitative analysis of the signals. Optical information is also processed to correct or avoid various kinds of distortion or noise, or transform them to a form more amenable to human perception. In the present time, digital computers and analog optical systems are used to process optical information (Ozaktas, 2021). However, the optical information is indicated by the amplitude or intensity of the light and less frequently, by the polarization and wavelength in analog optical information processing. Two variable amplitude light sources and one light meter are utilized to add two numbers optically while the multiplication of two numbers optically is expressed by the amplitude of the beam. Optical information processing is not only confined to a single pair of numbers to

be added or multiplied. Large arrays and high-resolution images are similarly processed and this is a unique advantage of optical information processing (Ozaktas, 2021; Goodman, 1968). With addition and multiplication in hand, any linear combination can be optically realized. This includes all linear systems and transformations, which can be acknowledged in the time it takes light to go through the system and be captured by the digital sensors.

The connection between coherent light propagation and the spatial frequency domain is the essence of analog optical information processing, and the area of analog optical information processing is referred to as 'Fourier optics'. The experiments of optical information processing to intentionally manipulate the frequency spectrum of a signal using Fourier optics have been performed by Abbe in 1873 and later by Porter in 1906 (Goodman, 1968). The sketch of the experimental configuration is shown in Fig. 1.1. A collimated, coherent light illuminates an object which is the letter "IIT BHU".

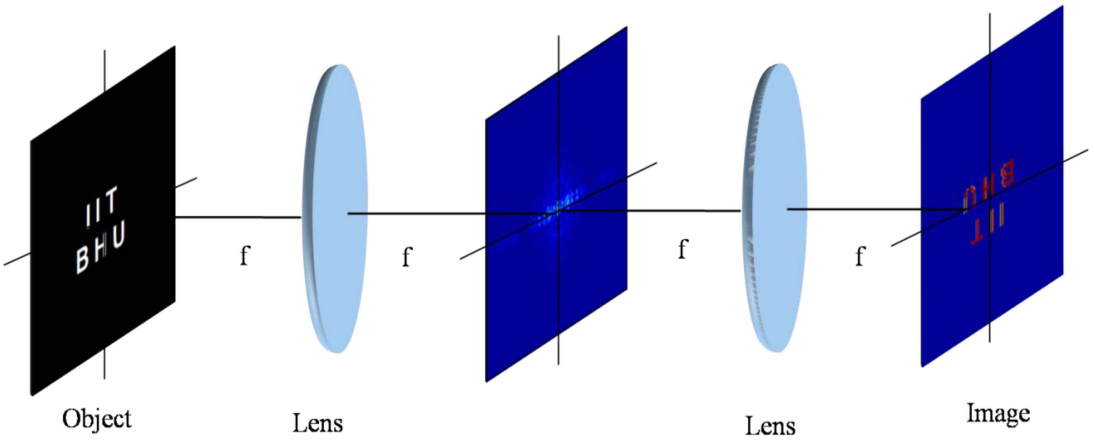

Fig. 1.1 Schematic for optical information processing**.**

A lens is placed to perform the Fourier transform of the object i.e letter "IIT BHU" and it appears at the back focal plane of the lens which is a Fourier spectrum of the object. Finally, the image at the imaging plane is obtained by recombining various

Fourier components as shown at the focal plane. The manipulation of the spectrum in a variety of ways is possible by introducing various obstructions (i.e an iris, a slit, a small stop, a soft customized aperture) in the focal plane of the lens. Fig. 1.2 (a) depicts an image of the spectrum of the letter "IIT BHU" corresponding to the full image shown in Fig. 1.2 (b). A series of isolated spectrum components at the focal plane of the lens generates due to the nature of the object, each spectrum spread somewhat by the finite extent of the circular aperture within which the object is confined. Each point at the focal plane represents the spatial frequency component of the signal and the frequency composition of the signal helps to understand and examine signal decomposition in terms of the plane waves.

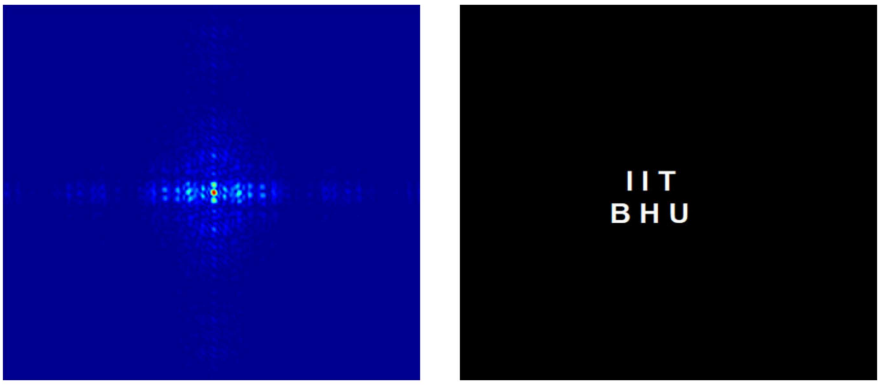

Fig. 1.2 (a) Shows the spectrum of the letter "IIT BHU", **(b)** represents the original image.

The ability of spatial filtering is well demonstrated by introducing a low pass filter in the focal plane which permits passing only low-frequency spectral components. Fig. 1.3 (a) represents the low pass filter at the Fourier plane to select the low-frequency components and Fig. 1.3 (b) is the image after filtering with a low pass filter.

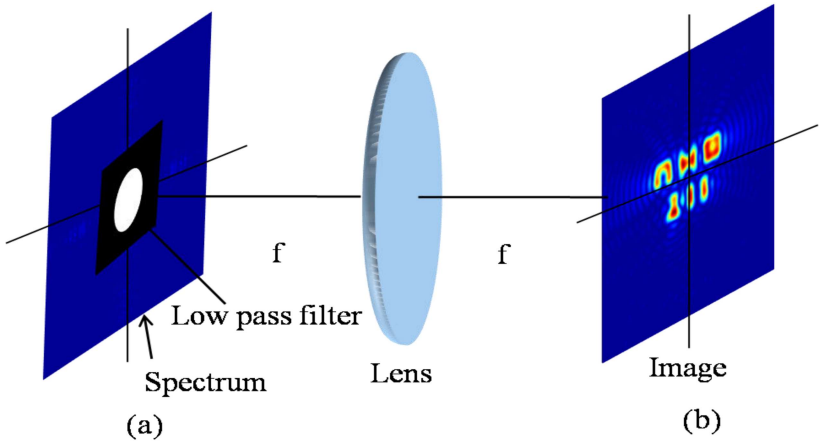

Fig. 1.3 Spatial filtering of the letter "IIT BHU" in the focal plane with the low pass filter **(a)** low pass filter at the focal plane, **(b)** representing the corresponding image.

1.2 Delivering optical information

In the previous section, we have seen how the composition of the frequency spectrum and their shaping determines the nature of the output signal and information contents. The light waves used to deliver optical information can be expressed on a different basis of frequency. One commonly used spectrum is explained in terms of the plane waves as described in Fig. 1.1. Apart from the plane wave decomposition, another emerging approach is using the OAM spectrum of the light, i.e., helical modes. The OAM basis has attracted significant attention in recent years in optical communication, imaging, OAM holography, image processing, etc. In order to explore optical signals into different bases, here we discuss two main methods namely (a) plane wave and (b) helical modes.

1.2.1 Plane-wave

The plane wave is the essence of Fourier optics. The spatial Fourier transform decomposes the light field into a composition of plane waves (Goodman, 1968). The plane wave plays a significant role in wave optics due to its simplest form and mathematical description. The wave with a plane wavefront at any moment of time, the

locations of constant phases are planes is referred to as a plane wave. The plane wave also has a uniform optical intensity across the plane wavefront (Hecht, 2012). A monochromatic plane wave is expressed as

$$E(r,t) = E_0 \exp\left[i\left(kr - \omega t\right)\right], \tag{1.1}$$

where r is the spatial coordinate. E_0 denotes the amplitude of the wave. k indicates wave number and ω is the frequency. A wavefront of a plane wave is shown in Fig. 1.4.

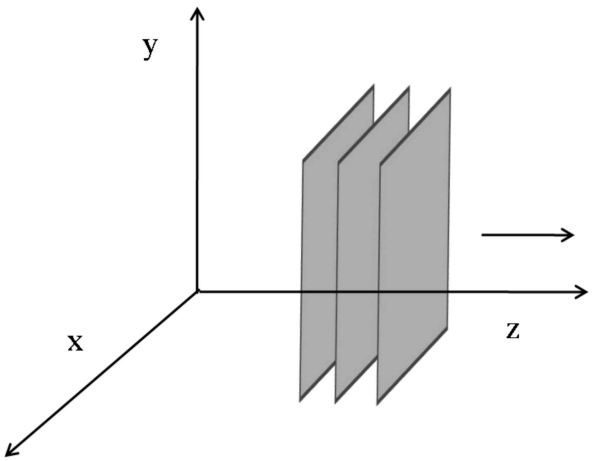

Fig. 1.4 Shows a plane wave.

1.2.2 Helical beam

A helical mode of light is characterized by a phase factor $\exp\left[il\varphi\right]$, where l is the topological charge and φ is the azimuthal angle (Allen, 1999; Torres, 2011; Zhan, 2009). This phase function features a screw dislocation that endows the beam with tremendous properties. First, The superposition of all phases along the axis results in destructive interference. The intensity of the helical beam redistributes into a ring-shaped structure under the paraxial approximation (Allen, 1999; Zhan, 2009). Second, the photons in the helical beam carry an orbital angular momentum (OAM) distinct from their spin angular

momentum (Torres, 2011). The light beam carrying OAM in free space, e.g., Laguerre Gaussian (LG) beams is shown in Fig. 1.5.

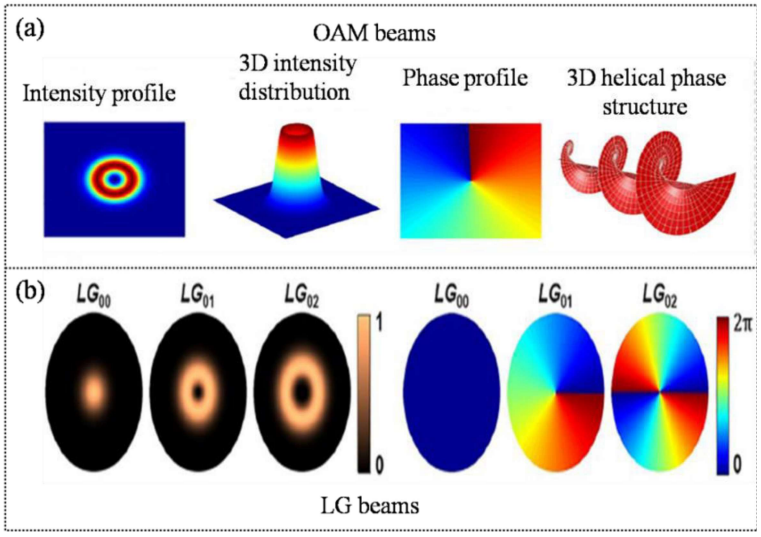

Fig. 1.5 (a) Shows OAM beams, **(b)** indicates LG beams.

1.3 Helical modes for the delivery of optical information

The physical dimension of a photon of light including frequency/wavelength, time, complex amplitude, polarization, and spatial structure (space) is shown in Fig. 1.6. These physical dimensions of light are used to encode and decode optical information to deliver from transmitter end to receiver end (Wang, 2016). The physical dimensions frequency/wavelength, time, complex amplitude, and polarization provide a limited degree of freedom for delivering optical information. On the other hand, the spatial structure of light i.e helical beam possesses a helical wavefront of the form $\exp[il\varphi]$, where l represents topological charge (TC). The sign of the TC is utilized to identify the handedness of the helix and the accumulated phase of the helical beam changes around the dark core in the order of $2l\pi$. The helical beam carries an orbital angular momentum (OAM) of $l\hbar$ per photon linked with the photon's helical wavefront (Torres, 2011). The

OAM modes *l* are theoretically infinite and orthogonal to one another in the Hilbert space (Allen, 2011; Wang, 2016; Yao, 2011).

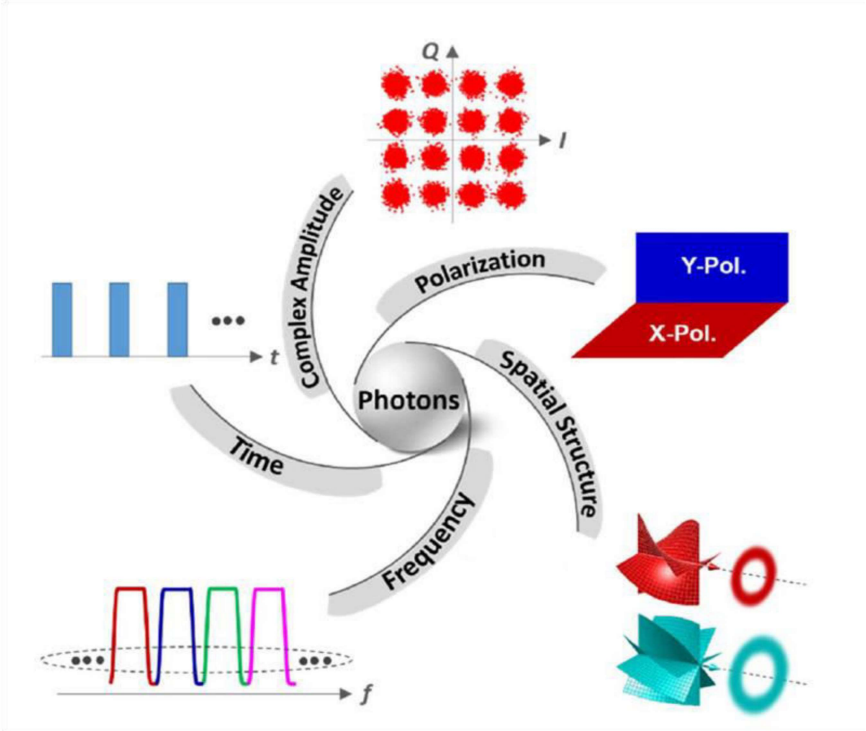

Fig. 1.6 Schematic representation of physical dimensions of photons (frequency/wavelength, time, complex amplitude, polarization, spatial structure) and orthogonal states (multiple wavelengths, time slots, constellation points in the complex plane, X- and Y-polarizations, phase vortices) (Wang, 2016).

Due to these significant features, the helical beam shows a higher degree of freedom for delivering optical information and can be used to encode and decode more than one optical information at a time using mode division multiplexing (MDM) (Willner, 2021). Moreover, OAM modes are useful in free-space optical communication as shown in Fig. 1.7. The OAM mode also maintains inter-channel orthogonality and minimizes crosstalk during free-space optical communication (FSO) (Willner, 2015, 2021). This can be accomplished by fully capturing the specific parameters that define the modal orthogonality. For instance, the different channels in FSO communication are defined by different OAM *l* values, the channel and OAM mode can be fully recovered by

azimuthally capturing a full 360^{o} circle no matter the size of the round aperture (Willner, 2021).

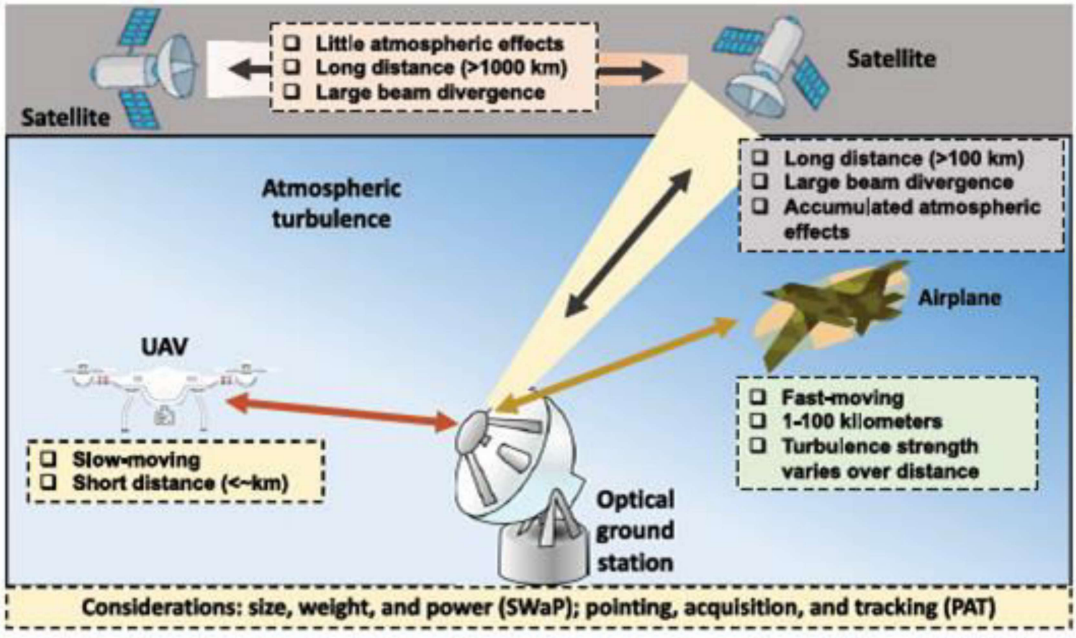

Fig. 1.7 Orbital angular momentum (OAM)-multiplexed free-space optical airborne and satellite communications (Willner, 2021).

1.4 Origin of helical beam

The term helical beam is used to represent the helical structure of a constant phase surface with a point of undefined phase and zero amplitude in the heart of the surface. This point is referred to as a 'singular point' and the beam is also referred to as a vortex beam. In addition, the accumulated phase change around this point is an integral multiple of 2π and this integral multiple is referred to as 'topological charge' l. The sign of the topological charge represents the handedness of the helix (Allen, 2016; Torres, 2011; Yao, 2011). A cophasal wavefront containing phase singular points has the form of a one or multi-start helical surface. The term singularity is not only confined to optical fields but has found importance in all two-dimensional fields described by a complex wave function (Berry, 2000; Nye, 1974). The significant investigation of optical phase singularity reported by

Nye and Berry (Nye, 1974) introduced a new branch of optics called "singular optics" Allen et. al. (Allen, 1999) demonstrated that the helical beam with a phase factor $\exp[il\varphi]$carries orbital angular momentum (OAM) of $l\hbar$ per photon. The helical beam can be obtained by solving Maxwell's equations in cylindrical coordinates under a paraxial approximation (Allen, 1999; Zhan, 2009).

Let us consider the wave equation for the electric field in a vacuum is represented as

$$\nabla^2\mathbf{E}-\frac{1}{c^2}\frac{\partial^2}{\partial^2 t}\mathbf{E}=0, \tag{1.2}$$

Eq. (1.2) is a scalar wave equation. Therefore, the solution of the wave equation can be written as

$$\mathbf{E}=Ee^{-i\omega t}, \tag{1.3}$$

Eq. (1.3) shows a monochromatic field. On substituting Eq. (1.3) into Eq. (1.2), therefore, Eq. (1.2) modifies as

$$\nabla^2 E+k^2E=0, \tag{1.4}$$

where k is a wave vector and represented as $k^2=\frac{\omega^2}{c^2}$. Eq. (1.4) is known as Helmholtz equation. For beams that are characterized by a small divergence angle with respect to the propagation direction, Eq. (1.4) can be investigated within the paraxial approximation. For a beamlike paraxial solution in cylindrical coordinates, the solution takes the following general formula

$$E(r,\varphi,z,t)=u(r,\varphi,z)\exp[i(kz-\omega t)], \tag{1.5}$$

Substituting Eq. (1.5) into Eq. (1.4) and considering the slowly varying envelope approximation leads to

$$\frac{1}{r}\frac{\partial}{\partial r}\left(r\frac{\partial u}{\partial r}\right)+\frac{1}{r^2}\frac{\partial^2 u}{\partial \varphi^2}+2ik\frac{\partial u}{\partial z}=0, \tag{1.6}$$

From this equation, the Laguerre–Gaussian modes can be calculated by using the separation of variables in r and φ (Allen, 1999; Zhan, 2009) as follows:

$$E(r,\varphi,z)=E_0\frac{\omega_0}{w(z)}\left[\frac{r\sqrt{2}}{\omega}\right]^l L_p^l\left(\frac{2r^2}{\omega^2}\right)e^{\frac{ikr^2}{2R(z)}}\exp\left[-i\varphi_{pl}(z)\right]\exp\left[il\varphi\right], \tag{1.7}$$

where $L_p^l(x)$ indicates the associated Laguerre polynomials that satisfy the differential equation and are represented as

$$x\frac{d^2L_p^l}{dx^2}-(l+1-x)\frac{dL_p^l}{dx}+pL_p^l=0,$$

and $\varphi_{pl}(z)=(2p+l+1)\tan^{-1}(z/z_0)$ represents the Gouy phase shift. E_0 is a constant and $w(z)$ represents beam spot size. *p=0, 1, 2,……*.is known as radial mode index and $l=0,\pm1,\pm2,.....$, called topological charge. L_p^l are the associated Laguerre polynomial. The lowest-order Laguerre Gaussian mode L_0^0 is identical to the Gaussian beam. The beam with zero radial order and azimuthal order l i.e L_0^l is referred to as a vortex beam shown in Fig. 1.8 and represented as

$$E(r)=E_l(r)\exp\left[il\varphi\right], \tag{1.8}$$

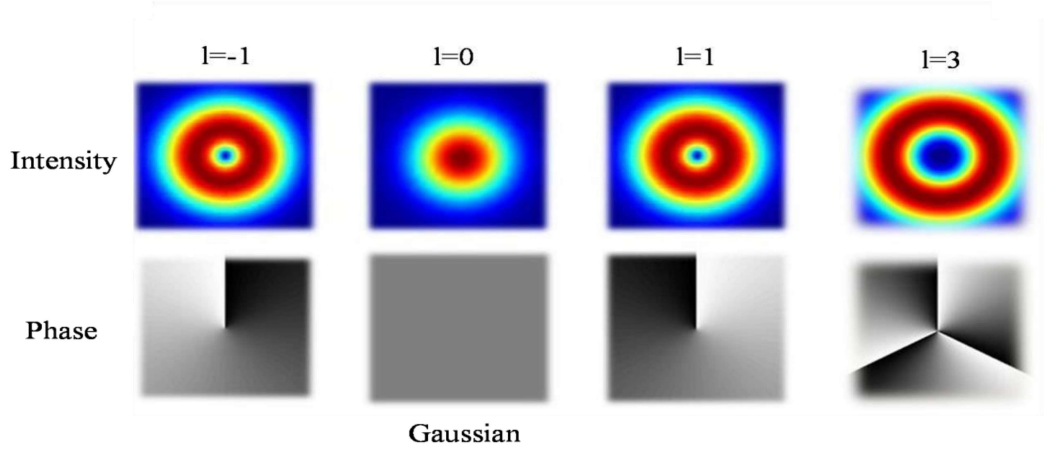

Fig. 1.8 Helical beams of different TC with their phase and intensity profile.

1.5 Generation of a helical beam

The helical beam can be achieved by shaping the spatial structure of the light in the desired fashion. There are several significant methods for the generation of vortex beams. Some vital techniques are discussed below.

1.5.1 Spiral phase plate

The characteristics of a helical beam are characterized by a twisted wavefront. The generation of a helical beam with a spiral phase plate (SPP) is the simplest and most direct technique. The SPP has a constant thickness in the radial direction and increases in the azimuthal direction, with a step height difference of h between the thinnest and thickest portion (Kotlyar, 2005) as shown in Fig. 1.9. The step height of the SPP is defined as $h = l\lambda\theta/\left[2\pi(n-n_0)\right]$, where n indicates the refractive index of the transparent dielectric material of the SPP while n_0 represents the refractive index of the external medium, λ is the wavelength of the incident light, l stands for topological (TC) charge and θ represents spatial azimuth. When the plane wavefront of the Gaussian beams is passed through the center of the SPP, then the spiral thickness of the SPP provides a different

phase in the azimuth direction in the incident light, resulting in a helical phase beam with TC *l* (Kotlyar, 2005).

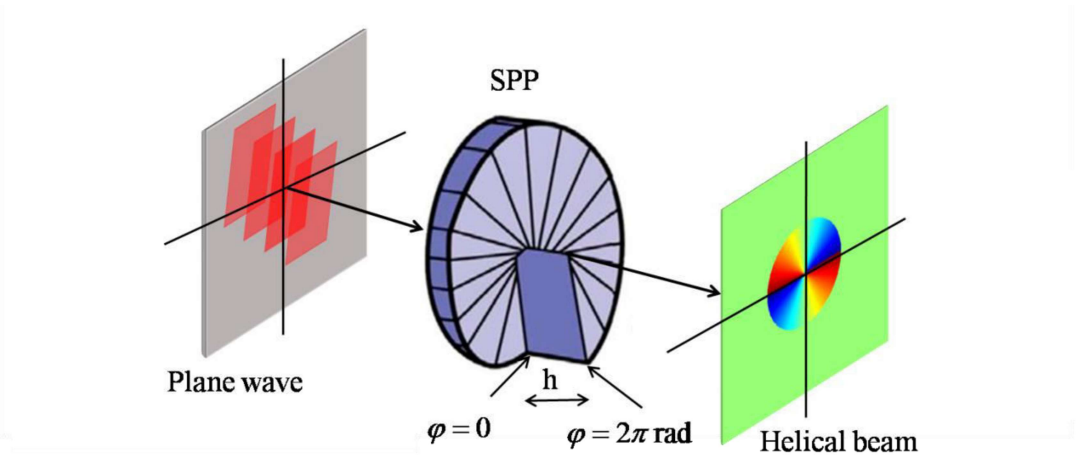

Fig. 1.9 Schematic of the generation of a helical beam with SPP.

1.5.2 Diffractive optical elements

The diffractive optical elements whose transmittance function is linked to the helical phase $\exp[il\varphi]$ are frequently used to generate the helical beams which can be designed using a computer-generated hologram as shown in Fig. 1.10. Holographic gratings, such as l-fold forked and Fresnel spiral diffraction gratings are designed using a photolithographic process by recording an interference pattern on a photoresist substrate or inserted in the path of the light beam using adaptable devices such as spatial light modulator (Li, S., 2013, Bai, 2022). When a plane wavefront of the Gaussian beam is passed through diffraction gratings then it generates a helical beam of TC *nl* in the non-zero diffraction order of the light (Li, S., 2013). Holographic gratings are relatively simple and fast helical beam generation methods, providing good wavefront flatness and higher efficiency.

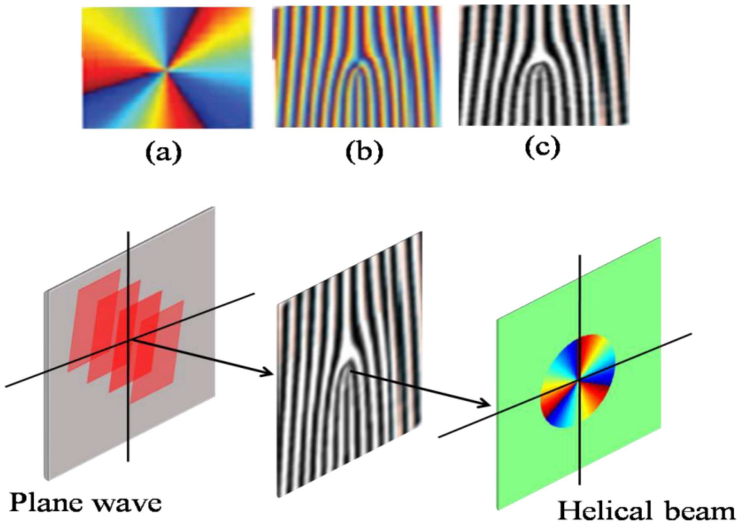

Fig. 1.10 Represents the phase hologram with l=3. **(a)** shows spiral phase hologram, **(b)** indicates l-fold forked hologram, **(c)** denotes binarized l-fold forked grating.

1.5.3 Spatial light modulator (SLM)

The SLM is used to generate a helical beam with different TCs and its highly advantageous due to the adaptable nature of the SLM. The SLM spatially modulates the coherent beam of light by the orientation of the liquid crystal molecules. The liquid crystal molecules of the SLM are programmed in such a way that it dynamically changes the parameters of the incident beam including the phase profile of the beam in the transverse plane (Efron, 1994; Maurer, 2011). The SLM can be utilized to generate and display a phase hologram with a transmittance function $\exp[il\varphi]$ by determining the phase value of each pixel in the 2D space according to the value of each pixel of the phase hologram. In order to generate a helical beam, the holographic gratings such as spiral phase hologram, l-fold forked hologram, and binarized l-fold forked hologram are displayed on the SLM (Bai, 2022; Shen, 2019; Yao, 2011) as depicted in Fig. 1.11.

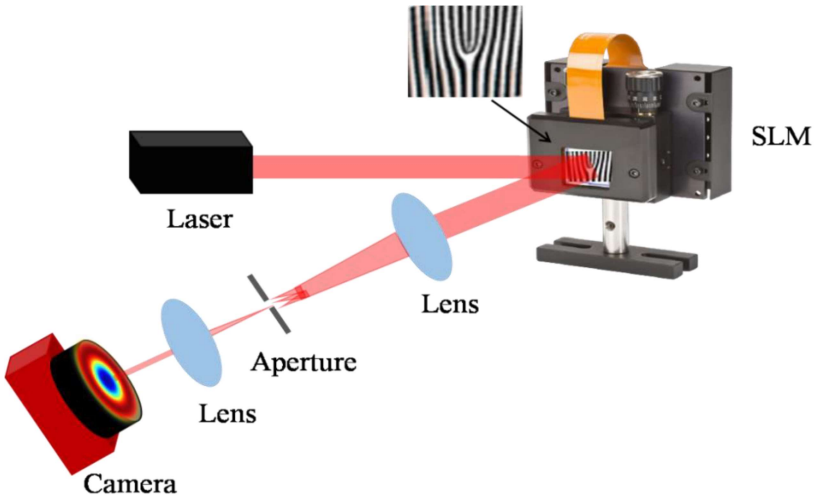

Fig. 1.11 Generation of vortex beam using SLM.

There are some other miscellaneous techniques for the generation of vortex beams including the use of a q-plate (Bai, 2022; D'Errico, 2017; Yao, 2011), metamaterials (Shi, 2017), mode conversion using cylindrical lenses (Courtial, 1999), and also manipulation inside the laser cavity (Huang, 2018), etc.

1.6 Detection of helical beam

The OAM detection at the receiver end is required in optical communication. The detection of helical beams is a significantly arduous task due to the deterioration of the OAM states during transmission. There are consequential approaches for the detection of helical beams. A few of them are discussed below.

1.6.1 Interferometric techniques

Interferometry is a commonly used technique to determine the wavefront of the helical beam and OAM modes. The interference of a tilted plane wave and a helical beam exhibits a fork-shaped interference pattern (Shen, 2019) as represented in Fig. 1.12. In this case, the formed interference pattern is similar to the forked grating with l-dislocation fringes as discussed earlier in section 1.5.2. The direction of the fringes depends on the

sign of the TC, and thus the OAM of the helical beam can be efficiently estimated. Moreover, when a coaxial plane wave superimposes with a helical beam, resulting in a petal-like interference pattern, the number of which is $|l|$ owing to the twisted phase $\exp[il\varphi]$.

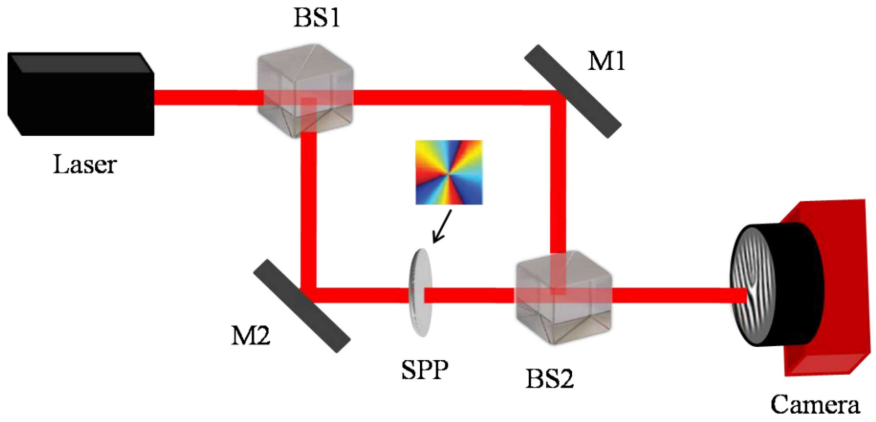

Fig. 1.12 Mach Zehnder configuration for measuring the OAM of the vortex beam. BS: Beam splitter, M: mirror, SPP: spiral phase plate.

On the other hand, the interference of a spherical beam and a helical beam forms helical fringes and the number of fringes is also l (Shen, 2019; Torres, 2011). The interferometric method includes the Mach-Zehnder interferometer (Leach, 2004), double-slit interference (Sztul, 2006), improved multipoint interferometer (Zhao, 2020), and lateral share interferometer (Ghai, 2008; Khajavi, 2018). Apart from these techniques, the combination of the Mach-Zehnder interferometer and Dove prisms were also utilized to measure the OAM modes (Leach, 2004).

1.6.2 Diffraction techniques

The diffraction pattern of a helical beam at the far field generated by diffractive elements is employed to detect the OAM of the helical beam. The measuring of the helical beam based on the diffraction methods is divided into the aperture diffraction method (Araujo,

2011, Melo, 2018; Princeton, 2019), the grating diffraction method (Ferreira, 2011; Li, 2020; Zhang, 2017), and cylindrical lenses (Miyamoto, 2019; Peng, 2015). When the helical beam is transmitted through a triangular or square aperture then it generates a diffraction pattern at the far field, the TC of the helical beam can be measured from this diffraction pattern (Araujo, 2019). The diffraction of a vortex beam by an aperture was first demonstrated by Hickmann et. al. (Hickmann, 2010). As shown in Fig. 1.13, the TC of the helical beam can be estimated from the diffraction pattern generated by a triangular aperture. Therefore, the TC of the helical beam of the incident beam is m=N-1, where N is the number of points on any side of the triangular lattice array.

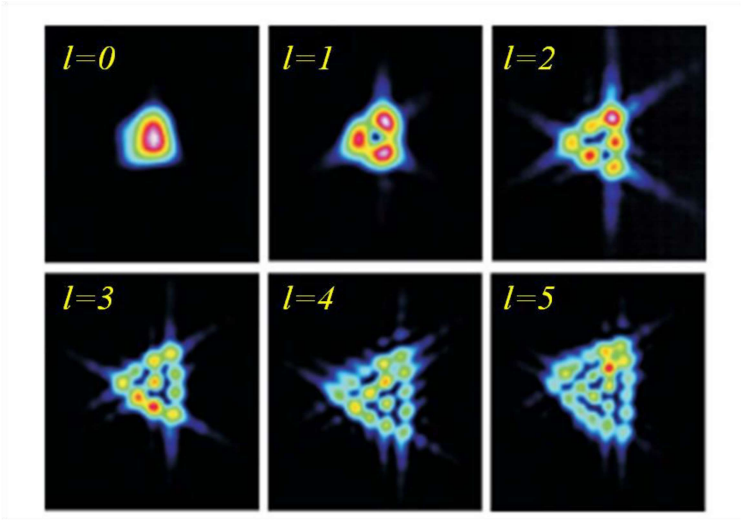

Fig. 1.13 Diffraction pattern of different helical beams at the far field using triangular aperture (Araujo, 2011).

The aperture of different shapes ranging from circular (Taira, 2017), diamond-shaped (Liu, Y., 2013), hexagonal (Liu, Y., 2011), and regular polygon (Ambuj, 2014) were also used in diffraction experiments to detect helical beams.

1.6.3 Deep learning

Deep learning methods have been widely used in recent years in the regime of image processing with their powerful advantages of information processing and data analysis using a local connection, shared weight, pooling, and multilayer structure (Knuston, 2016; Li, 2017; Park, S., 2018). Usually, a neural network consists of convolutional layers, pooling layers, and fully connected layers. The convolutional layers are implemented to detect the local combination features from the previous layers, the pooling layers merge semantically similar features into one, and the fully connected layer is utilized to realize the classifications. By adopting this analogy, helical beam measurement based on a convolutional neural network (CNN) has gradually emerged in recent years (Knuston, 2016; Li, 2008, 2017; Park, S., 2018).

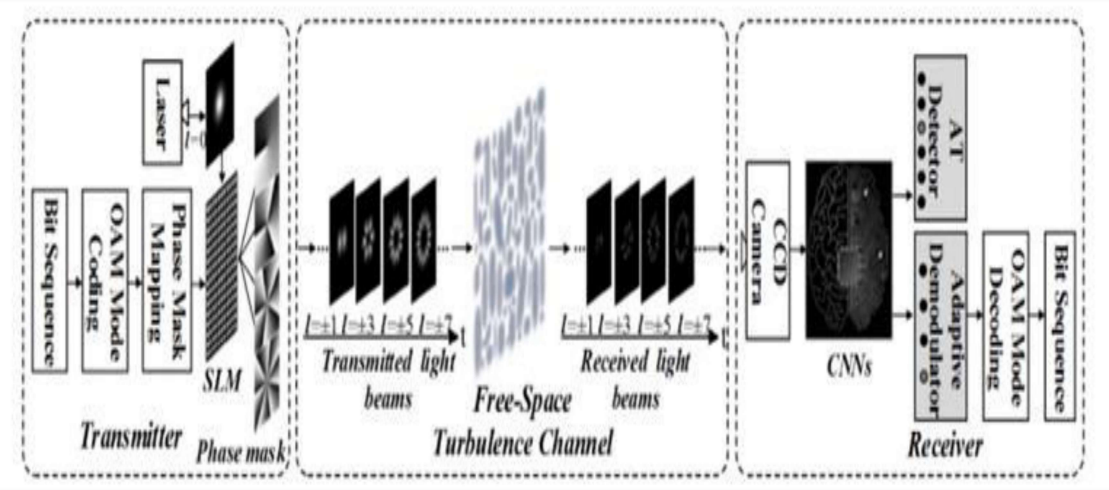

Fig. 1.14 The learning model for helical beam detection (Li, 2008).

Li et. al. [Li, 2008] developed a multi-layer learning method to recognize the OAM modes of multiple vortex beams with high accuracy under different atmospheric turbulence as shown in Fig. 1.14. The different helical beams are transmitted through the turbulence channel. The captured intensity images at the detection plane are resized to

speed up the training process, then convolutional layers are used to extract image features, pooling layers comprise the dimensions, and finally, fully connected layers provide the output result. Other vital methods include the use of twisted phase elements (Shen, 2019), hyperbolic grating (Liu, 2018), axicon (Han, 2011), spiral spectra (Ni, 2017), single point detector (Li, S., 2018), Talbot effect (Panthong, 2018), and Shack-Hartmann sensors (Chen, M., 2017). Apart from these methods, some techniques to sort OAM models have also been reported (D'Errico, 2017; Litvin, 2012; Pinnell, 2020; Schulze, 2013).

1.7 Applications of helical beam

1.7.1 Optical communication

Similar to other physical dimensions of light such as frequency/wavelength, complex amplitude, time, and polarization, the OAM mode is an attractive feature of the light for optical communication (Wang, 2016; Willner, 2015, 2021). The two techniques either the OAM modulation scheme or OAM multiplexing methods can be exploited for optical communication (Willner, 2015) as shown in Fig. 1.15. As shown in Fig. 1.15 (a), time-varying phase modulation uses different phase vortex beams to denote different data information. Two-phase vortex states correspond to binary data information (e.g +1 for 1 and -1 for 0), while multiple-phase vortex indicates data information. On the other hand, different phase helical modes (e.g +1 and -1) are implemented for multiplexing and used as independent carriers to transfer different channel data information (Wang, 2016). The binary on-off keying (OOK) is employed to modulate each channel data information. The multiplexing of multiple channels carried by the phase vortex beams can increase the transmission capacity and spectral efficiency as depicted in Fig. 1.15 (b).

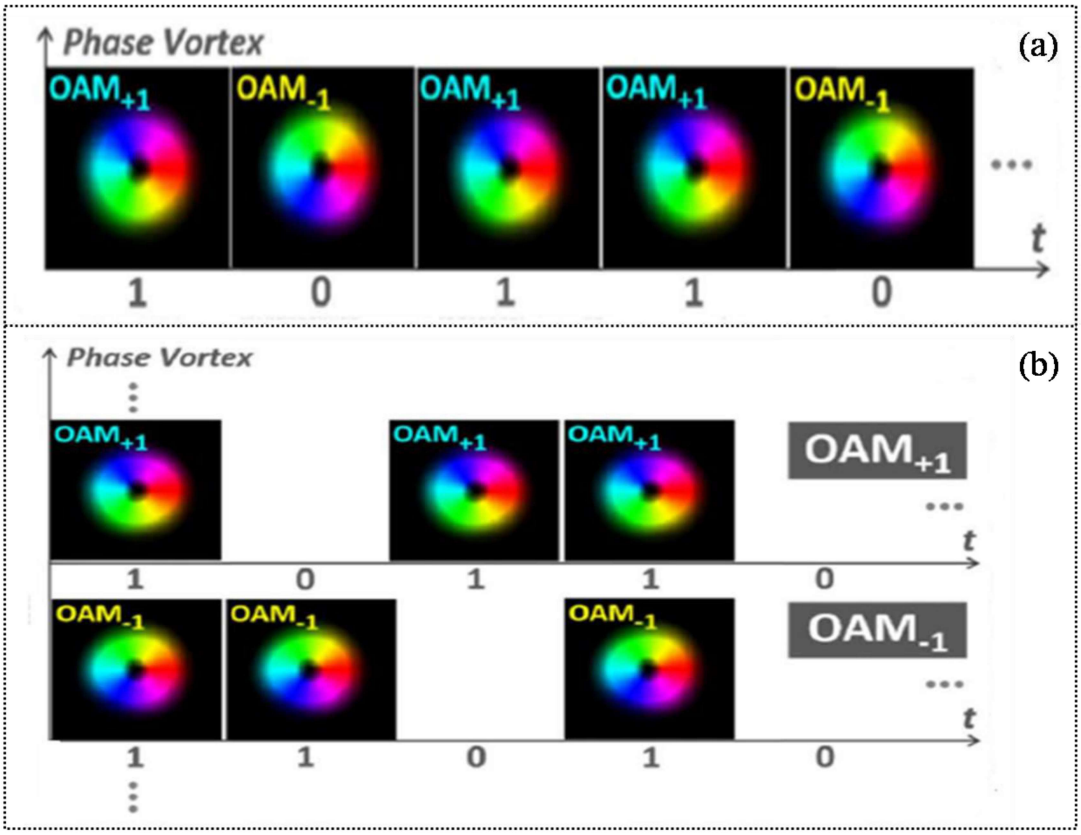

Fig. 1.15 Schematic of optical vortex modulation and multiplexing (Wang, 2016).

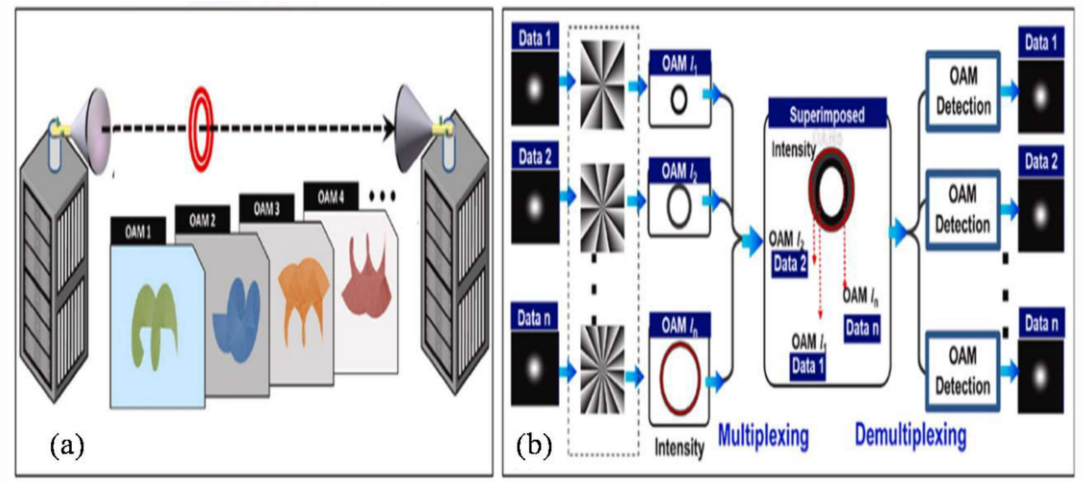

Fig. 1.16 (a) Multiple OAM beams are coaxially transmitted through free space. **(b)** Each orthogonal OAM beam carries an independent data stream (Willner, 2021).

On the other hand, Fig. 1.16 (a) shows the FSO communication using helical modes (Willner, 2021). Fig. 1.16 (a) indicates the coaxial transmission of multiple helical

modes through the free space. In Fig. 1.16 (b), each orthogonal helical mode with $+l$ value carries an independent data stream and superimposed all the helical modes using multiplexing at the transmitter end, and the data streams are decoded at the receiver end by demultiplexing of helical modes with different $-l$ values.

1.7.2 High-resolution imaging

The helical beam shows unique features due to its helical wavefront and doughnut intensity pattern (Allen, 2016). This unique feature of the helical beam can be utilized to develop high-contrast and high-resolution imaging systems (Chen, 2014; Rittweger, 2009; Wang, 2022).

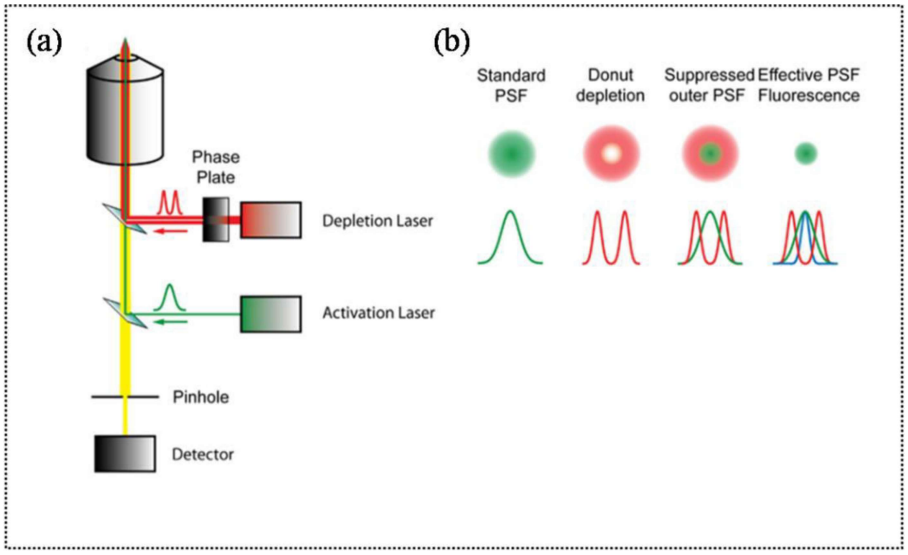

Fig. 1.17 (a) Represents a sketch of STED**, (b)** denotes effective PSF (Hiersemenzel, 2013).

A new imaging technique has been proposed, called digital spiral imaging, to enlarge the resolution using the analysis of the OAM modes of the helical beam (Chen, 2014). Recently, the OAM mode of the vortex beam has been analyzed to develop a super-resolution imaging system (Wang, 2022). The helical phase of the helical beam is also employed to develop and design a super-resolution microscopy named stimulated

emission depletion microscopy (STED) (Rittweger, 2009) as depicted in Fig. 1.17. In the STED, two lasers are used in the focal plane i.e excitation laser and depletion laser. The depletion laser is generated by passing a plane wavefront of a Gaussian beam through the spiral phase plate (SPP). When these two lasers are used together, the excitation laser and the depletion laser reduce the effective point spread function (PSF) and provide high resolution.

Some other interesting applications of the vortex beam can be seen in optical tweezers, metrology, biomedicine, OAM holography, and optical machining (Feng, 2020, Rittweger, 2009; Shen, 2019; Wang, 2022; Yao, 2010).

1.8 Optical information using holography

Holography plays a significant role in the delivery of 3D optical information owing to the capability of recording and reconstructing the complex field, i.e., amplitude and phase of the light (Gabor, 1948; Leith, 1962). The complex field information is recorded into a hologram by the interference of the unknown optical field and reference waves. Recording of the hologram by a digital detector and numerical reconstruction of the hologram has revolutionized holography and the technique is referred to as digital holography (DH) (Poon, 2006; Hariharan, 2002). DH with different geometries have been used, and vital among them are in-line (Gabor, 1948), off-axis (Leith, 1962), and phase-shifting (Yamaguchi, 2006, Micó, 2009) depicted in Fig. 1.18.

Consider an interference of coherent waves coming from an object $E_o(r)$ and reference $R(r)$ at the detection plane as shown in Fig. 1.18. The intensity at the observation plane is denoted as

$$I(r) = |E_o(r) + R(r)|^2 \tag{1.9}$$

Eq. (1.9) can be written as

$$I(r) = |E_o(r)|^2 + |R(r)|^2 + E_o(r)R(r)^* + E_o^*(r)R(r), \quad (1.10)$$

where asterisk * indicates the complex conjugate and *I(r)* represents the hologram. It consists of three terms: the 0-order is composed of $|E_o(r)|^2 + |R(r)|^2$, the +1 order is represented by $E_o(r)R(r)^*$, and the -1 order is $E_o^*(r)R(r)$.

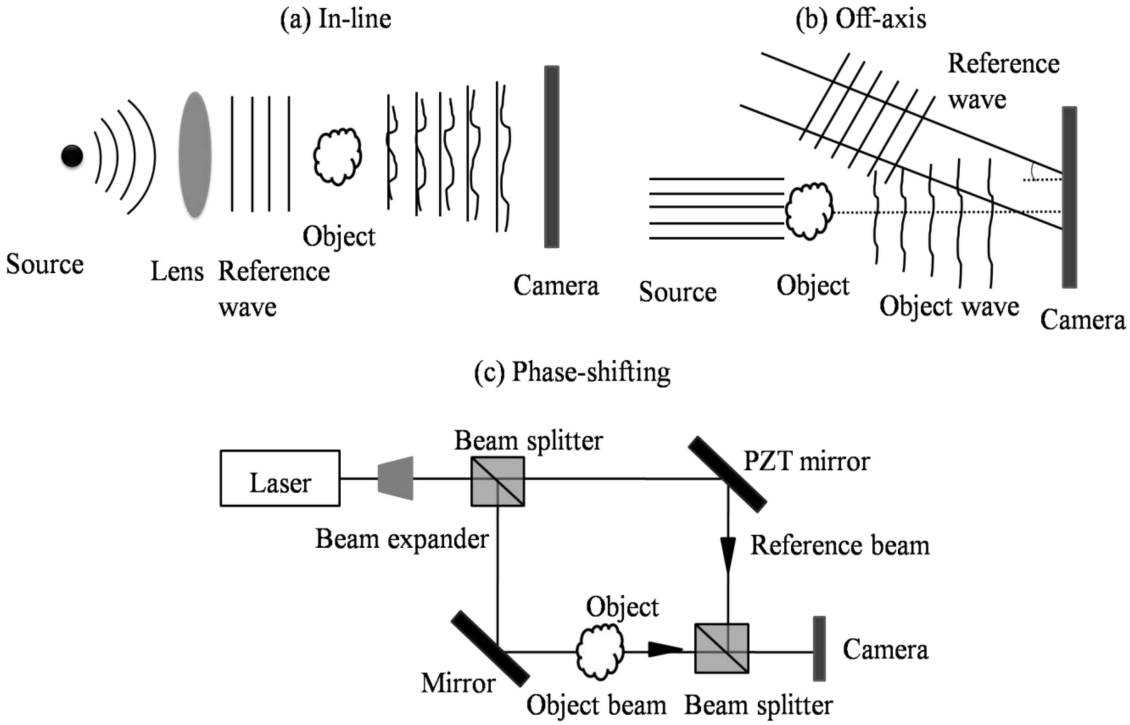

Fig. 1.18 Basic geometries for holography.

The in-line holography faces a twin image problem and it is difficult to directly separate these three terms and distinguish the object shown in Fig. 1.18 (a). The twin image issue of in-line holography is circumvented by providing an angular separation to the reference beam in the off-axis holography represented in Fig. 1.18 (b). However, the field of view (FOV) is constrained due to the limited pixel size in the image sensors and sharing of the frequency space (Gross, 2008). To resolve the issue of off-axis holography and enhance

the field of view, phase-shifting holography has been proposed as depicted in Fig. 1.18 (c). A phase-shifting holography approach is implemented by recording several images with phase shifts between the consecutive images. Phase shift is introduced into an object or reference waves by a liquid crystal phase modulator (Kadono, 1994), a piezoelectric transducer (Yamaguchi, 2006), or an acousto-optic modulator (Sung, 2009).

Apart from these developments, common path experimental geometries have also been proposed to develop compact and highly stable DH techniques (Micó, 2010; Shaked, 2012; Mahajan, 2015; Varghese, 2018). Extension of the DH to the polarization regime has been reported in recent years for recording and reconstruction of the complete wavefront of the light (Lohmann, 1965; Colomb, 2002; Nomura 2007). Moreover, the application of polarization digital holography to the Jones matrix imaging has been applied to examine light-matter interactions with coherent light (Popescu, 2006, Sreelal, 2017; Park, 2021).

The physical dimensions of light, including frequency/wavelength, time, and polarization are used to carry independent information channels for high-capacity holographic systems. On the other hand, The OAM mode of the helical beam which is theoretically unlimited has emerged as a new degree of freedom for boosting optical information capacity (Willner, 2015, 2021). Therefore, the OAM mode of the helical beam has been demonstrated to develop OAM holography for holographic multiplexation and high-security information by implementing the OAM mode as an information carrier (Feng, 2020). The OAM holography has the potential in reconstructing multiple OAM-carrying images, without a theoretical limit of the OAM modes. In OAM holography, first, an ordinary digital hologram is sampled in its spatial frequency domain and the spatial frequency bandwidth of the incident OAM mode which obeys a doughnut-shaped

intensity profile is used to determine the sampling period. To maintain the OAM selectivity, a helical phase should be encoded onto the hologram. An OAM hologram can henceforth be created for high-security optical encryption. Further, the helical phase has been modulated by a cosine function and is referred to as modulated orbital angular momentum (MOAM) which shows the additional degree of freedom and improved the performance of OAM holography (Wang, 2022). This is realized by imposing multiple modulation phase modes into one OAM mode.

1.9 Optical information delivery through randomness

Optical information delivery and recovery with random scattering media has long been a challenge and yet a highly practical issue, as scattering corrupts light's wavefront.

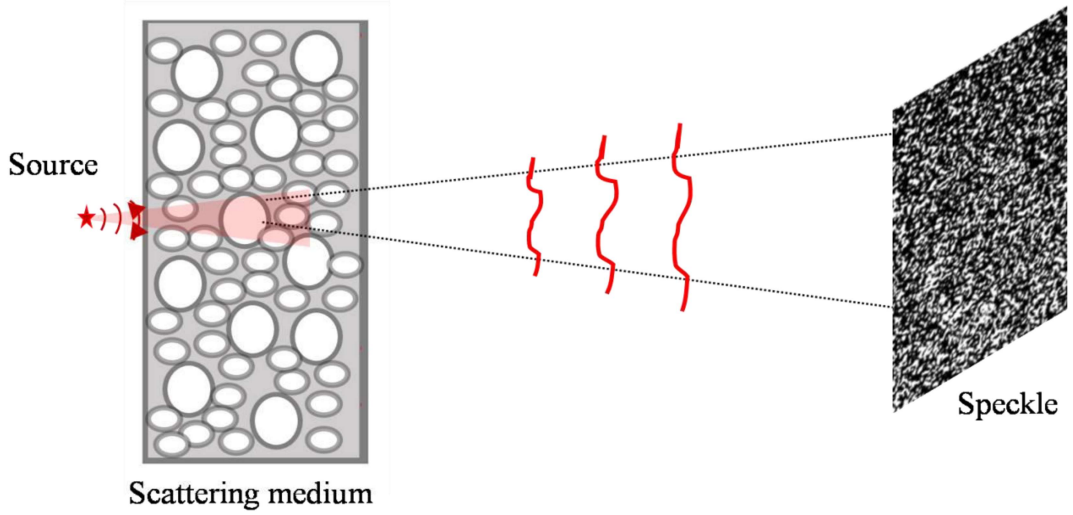

Fig. 1.19 Generation of the speckle pattern.

When coherent light propagates through a non-absorbing opaque medium or scattering media, the light gets randomization and the wavefronts of the light get scrambled due to the inhomogeneity of the optical path length in the scattering media. It further aggravates coherent noise owing to the statistical interference of randomly scrambled waves is referred to as speckle (Dainty, 1984; Goodman, 2007) as shown in Fig. 1.19. The speckle

pattern is generated due to the random scattering of coherent light by the inhomogeneous media. This random pattern does not provide any direct access to optical information as shown in Fig 1.20. Fig. 1.20 (a) shows the co-axial propagation of the composition of the OAM modes of the helical beams for delivery of the optical information through the scattering media. The scattering media in the propagation channel scatters these incident spatial modes and leaks one mode into another mode (Gong, 2019, Willner, 2021).

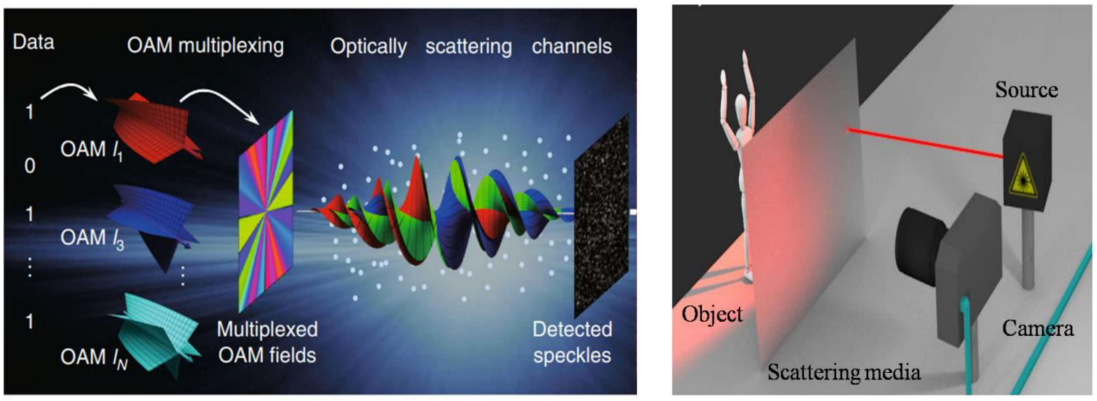

Fig. 1.20 (a) Co-axial propagation of OAM modes for delivery of optical information (Gong, 2019), **(b)** imaging of hidden object behind the random scattering media.

Due to these reasons, the detection and sorting of vortex beams become more difficult. On the other hand, seeing a target obscured by the random scattering media and a non-line of sight (NLOS) imaging are some of the challenging issues as depicted in Fig. 1.20 (b). However, randomly scattered light fields reaching the detector carry the signature of the information of incident light. The grainy structure of the speckle pattern at the observation plane possesses enough information about the scattering media and proper evaluation and use of this random light can be used to design and develop new tools and techniques for information optics and imaging through scattering media. A few techniques have been investigated to overcome this scattering effect, at least to some extent by using phase conjugation, transmission matrix, adaptive optics method, etc. On the other hand, the correlation optics-based method relies on using the randomness of the

light (rather than canceling it) to recover the desired information from the randomly scattered light. Some of these methods to deliver and recover optical information through random scattering media are explained below.

1.9.1 Optical phase conjugation

Optical phase conjugation (OPC) is a technique where an incoming light is reflected with a reversed-phase or phase-conjugated wave, and used to remove the effect of aberrations.

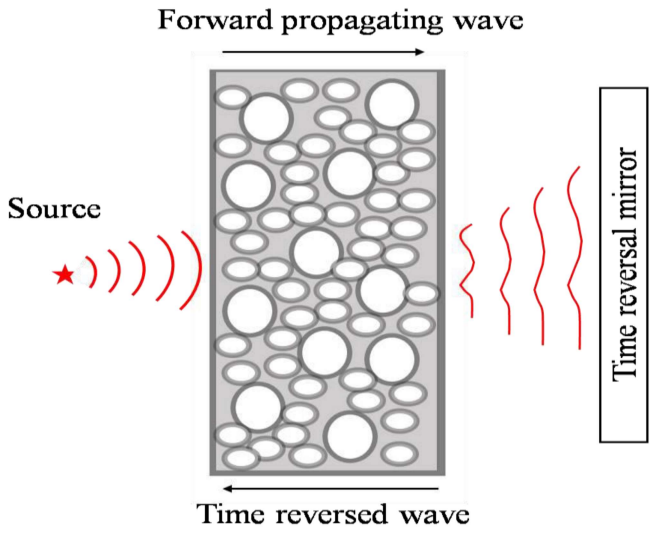

Fig. 1.21 Schematic of OPC.

Optical phase-conjugated waves are generated using various non-linear optical processes (such as four-wave mixing, three-wave mixing, backward stimulated scattering, and others) (Guan, 2012; Nixon, 2013; He, 2013; Horstmeyer, 2015, Park, 2018). This is also generated through one photon and multi-photon pumped backward stimulated emission process in a lasing medium. The most significant practical applications of OPC appear to be in wavefront corrections. A schematic of OPC is shown in Fig. 1.21. A phase conjugate reflector is introduced to generate a backward wave having a reversal wavefront distribution with respect to the propagation direction. Further, phase conjugation has also been reported digitally by combining a digital holography approach

with dynamic computer-generated holography employing a spatial light modulator (SLM) (Baker, 2004; Mao, 1991). This technique is referred to as digital phase conjugation and has the potential to be fast phase conjugation through a random scattering media.

1.9.2 Optical memory effect

Angular memory effect or simply the memory effect principle states that two objects in close vicinity or separated by a small separation θ, generate identical speckles at the observation plane except for a lateral shift (Freund, 1990; Osnabrugge, 20170. A lateral shift in the transmitted beam arises due to any angular shift in the incident beam as depicted in Fig. 1.22. Further, the principle of memory effect of the scattering media has been exploited to develop imaging techniques through the scattering media (Bertolotti, 2012, 2014; Katz, 2012, 2014). The memory effect was combined with autocorrelation of the intensity to reconstruct the image of the object from the random light (Katz, 2012, 2014). These techniques utilize the autocorrelation of the intensity speckle pattern with phase retrieval to recover information from the randomness.

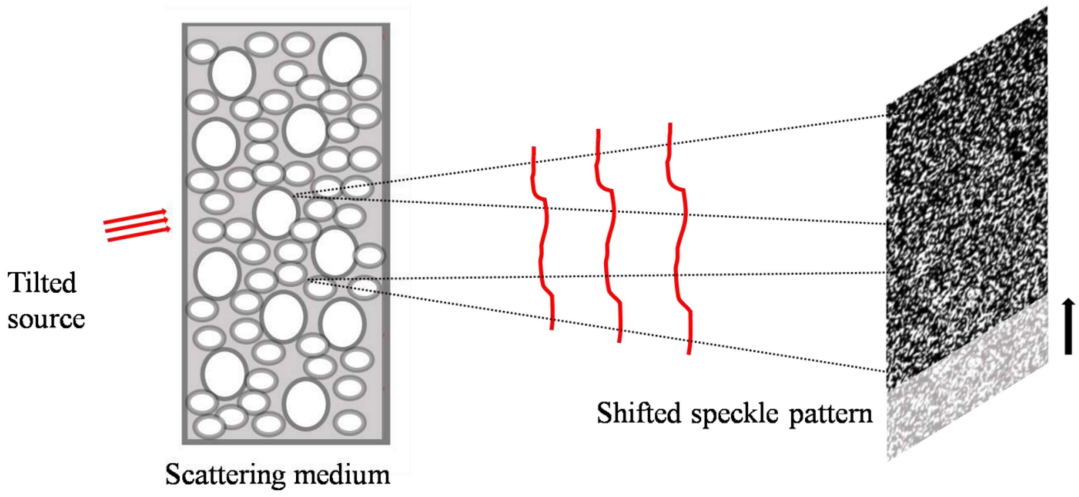

Fig. 1.22 Schematic of the memory effect: an incident-tilted source results in the shift of the speckle pattern in the observation plane.

1.9.3 Correlation optics approach

In order to use the randomness of the light for information optics and imaging, fundamental features of the random light such as the two-point complex coherence function can be utilized. For instance, the random light that follows Gaussian statistics can be characterized by the complex-coherence function i.e correlation at two points in space or time. The seminal work and foundations by Emil wolf on coherence optics have provided significant background and theoretical bases to explore correlation-based methods (Wolf, 2007). The van-Cittert Zernike (vCz) theorem and the Hanbury Brown Twiss (HBT) experiment are two central results in the coherence optics. The vCZ theorem establishes a connection between an incoherent source and a complex coherence function at the far field (Goodman, 2007; Gori, 1998; Wolf, 2007). On the other hand, the HBT is a powerful and fascinating approach to characterizing random light fields by intensity correlation. The HBT utilizes the connection between the second and fourth-order Gaussian random field to evaluate the complex coherence function in a simple experimental method. The work of HBT led to innovations of several methods in the classical domain and quantum optics. Further, the HBT approach was used to develop significant inventions in the fields of speckle contrast imaging (Briers, 2013; Bromberg, 2010; Hassinen, 2011; Kumar, 2012; Singh, R., 2014), high energy physics, nuclear physics, and atomic physics (Wiedemann, 1997). In context to characterize the random fields, the different methods are discussed in the upcoming section.

1.9.3.1 The complex coherence function

The complex coherence function measures the degree of statistical similarity of the random scattered field at two different positions or times.

The scattered field at the observation plane situated at the far field, for a fixed time t is represented as

$$E(r) = \int E(\hat{r}) \exp\left[i\delta(\hat{r})\right] \exp\left(-i\frac{2\pi}{\lambda f} r.\hat{r}\right) d\hat{r}, \tag{1.11}$$

where $\hat{r}$, r indicate the spatial position vectors at the source and observation planes. $\delta(\hat{r})$ is the random phase acquainted by the random scattering media. λ represents the incident wavelength and f is the focal length of the lens as represented in Fig. 1.23.

The complex coherence function or the mutual intensity at the observation plane is represented (Singh, 2013) as

$$W(r_1, r_1 + \Delta r) = \left\langle E^*(r_1) E(r_1 + \Delta r) \right\rangle$$

$$W(r_1, r_1 + \Delta r) = \int \left\{ \iint E_1^*(\hat{r}_1) E_2(\hat{r}_2) \exp\left[-i(\delta(\hat{r}_1) - \delta(\hat{r}_2)\right] \times \exp\left[-i\frac{2\pi}{\lambda f}((r_1 + \Delta r).\hat{r}_2 - r_1.\hat{r}_1) d\hat{r}_1 \right.\right.$$

$$\left.\left. d\hat{r}_2 \right]\right\}_J dr_1, \tag{1.12}$$

Taking into account of the delta function resulting from the spatial averaging in the observation plane given by $\int \exp\left(-\frac{ik}{f}(\hat{r}_2 - \hat{r}_1).r_1\right) dr_1 = \delta(\hat{r}_2 - \hat{r}_1)$, Eq. (1.12) modifies to

$$W(\Delta r) = \int I(\hat{r}_1) \exp\left(-\frac{ik\Delta r.\hat{r}_1}{f}\right) d\hat{r}_1, \tag{1.13}$$

where $I(\hat{r}_1) = E^*(\hat{r}_1) E(\hat{r}_1)$ is the intensity at the source plane. Eq. (1.13) states that the complex coherence function at the observation plane is the Fourier transform of the source at the random scattering plane and is known as a spatial version of the van-Cittert Zernike theorem.

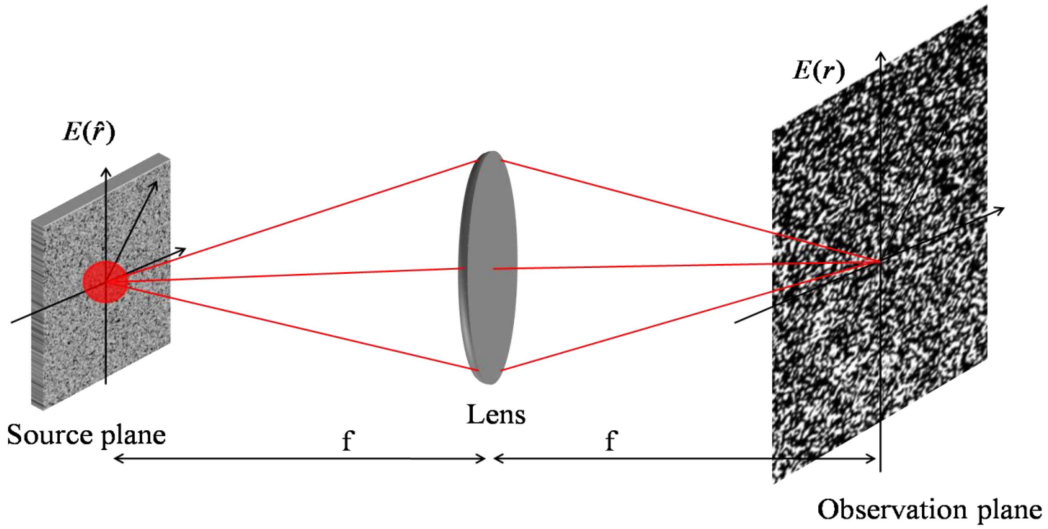

Fig. 1.23 Schematic for the scattering of coherent light from a random scattering media and generation of the randomly scattered field at the observation plane.

1.9.3.2 Intensity correlation

The mutual intensity of the light field plays a very significant role in light characterization and imaging. For instance, the mutual intensity of the field has been used to determine the stellar size in the early 20th century. Though the experimental measurement of the mutual intensity is susceptible to external disturbances and it has opened door to several new ideas on imaging through the second-order correlation of the field (Takeda, 2005, Borghi, 2006; Wang, 2009). Hanbury Brown & Twiss (HBT) approach to use the correlations of the intensity fluctuations, i.e., the fourth-order field correlations brought a major breakthrough in the characterization of the light fields (Mandel, 1995, Brown, 2013; Magaña-Loaiza, 2016). The intensity correlations of the light field unravel several unique and unknown features which were missing in the second-order interferometer. The intensity correlations made an immense impact in astronomy, astrophysics, and correlation-based imaging. Recently the correlation of entangled photons in quantum ghost imaging schemes has been utilized to understand the depth information of the quantum light (Erkmen, 2010; Shapiro, 2012; Padgett, 2017). In comparison to the

interferometers with second-order field correlation, the interferometers based on fourth-order correlations are rather simple and free from instability due to external disturbances (Bromberg, 2010; Brown, 2013; Singh, R., 2014; Vinu, 2020, Chen, 2020). A sketch diagram to measure the quantity of interest associated with intensity correlation is shown in Fig. 1.24.

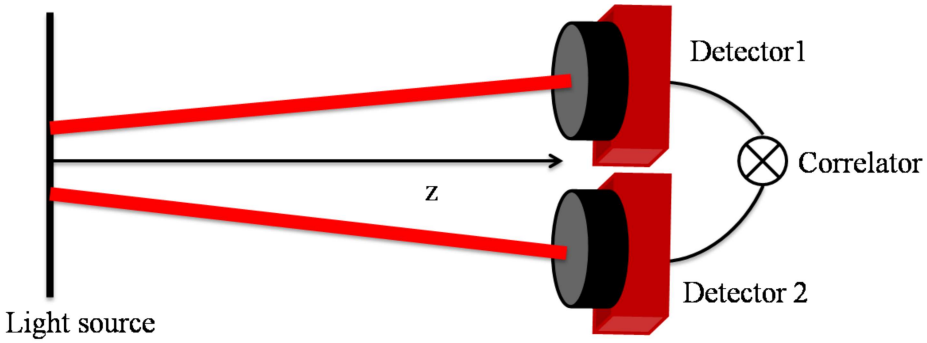

Fig. 1.24 Schematic diagram for intensity correlation measurement.

The mathematical basis of the intensity correlations of the stochastic light field is explained below and details can be also found in Ref. (Goodman, 2007, Bromberg, 2010; Brown, 2013). The correlation function $g^{(n)}$ measures correlation at any arbitrary position or time. Here, the separation of points in space is considered for further calculation. The first and second-order correlations $g^{(1)}$ and $g^{(2)}$ are of special interest. The first-order correlation function $g^{(1)}$ is expressed as

$$g^{(1)}(r_1, r_2) = \left\langle E^*(r_1) E(r_2) \right\rangle, \tag{1.14}$$

where r_1 and r_2 are the two separated points in space. The angular bracket represents the ensemble average.

The fourth-order field correlation is denoted as

$$g^{(2)}(r_1, r_2) = \langle E^*(r_1) E(r_2) E^*(r_2) E(r_1) \rangle, \tag{1.15}$$

Substituting $I = E^* E$ into Eq. (1.15), therefore Eq. (1.15) modifies to

$$g^{(2)}(r_1, r_2) = \langle I(r_1) I(r_2) \rangle, \tag{1.16}$$

The correlation of intensities can be estimated either electronically or digitally. The fourth-order correlation can be written in terms of second-order correlation by utilizing the Siegert relation as

$$\langle I(r_1) I(r_2) \rangle = \langle I(r_1) \rangle \langle I(r_2) \rangle + |E^*(r_1) E(r_2)|^2, \tag{1.17}$$

Therefore,

$$g^2(r_1, r_2) = \langle I(r_1) \rangle \langle I(r_2) \rangle + |g^1(r_1, r_2)|^2 \tag{1.18}$$

Eq. (1.18) highlights that the fourth-order correlation can be explained in terms of the amplitude of the second-order correlation. Further, the intensity autocorrelation of the speckle pattern has been demonstrated to develop imaging systems through random scattering media (Bertolotti, 2012, 2014; Katz, 2012, 2014). The intensity autocorrelation only provides the amplitude information of the object while phase information of the complex coherence function is lost. However, recovery of phase in the intensity correlation is possible by combining the holography principle with the coherence wave interference (Singh, R., 2014, 2017).

1.9.3.3 Characterization of vectorial random field

The vectorial representation of statistical features of the optical field attracts the great attention of researchers after the development of the unified theory of coherence and polarization in a common framework (Wolf, 2007). The two-point correlation either in space or time of the random field is referred to as coherence while the correlation of the vector state of the field at the same point is referred to represent polarization. In recent

years, many investigations have been reported to control synthesizing the coherence and polarization features of the random fluctuating field and the potential of random polarization speckles (Broky, 2010; Kumar, 2022; Takeda, 2010) as represented in Fig. 1.25 as a versatile tool in controlled synthesis. The random phase screen and liquid crystal spatial light modulator were utilized to modulate coherence and polarization properties (Ostrovsky, 2009; Shirai, 2004). The vectorial random field was controlled and synthesized by employing the extension of coherence holography in the vectorial regime (Singh, R., 2017; Takeda, 2010). Moreover, the state of polarization of a light field is represented by a polarization ellipse or the Poincare sphere representation. The state of polarization of a coherent light field at a single point can be explained by the Stokes parameters (SPs) as defined below

$$
\begin{aligned}
S_0(r) &= E_x^*(r)E_x(r) + E_y^*(r)E_y(r), \\
S_1(r) &= E_x^*(r)E_x(r) - E_y^*(r)E_y(r), \\
S_2(r) &= E_x^*(r)E_y(r) + E_y^*(r)E_x(r), \\
S_3(r) &= i\left[E_y^*(r)E_x(r) - E_x^*(r)E_y(r), \right],
\end{aligned}
\tag{1.19}
$$

Experimental measurement of the polarization state of the field is possible by SPs measurement (Goldstein, 2017, Schaefer, 2007) or by the interferometric method for coherent light (Naik, 2012, Vinu 2015).

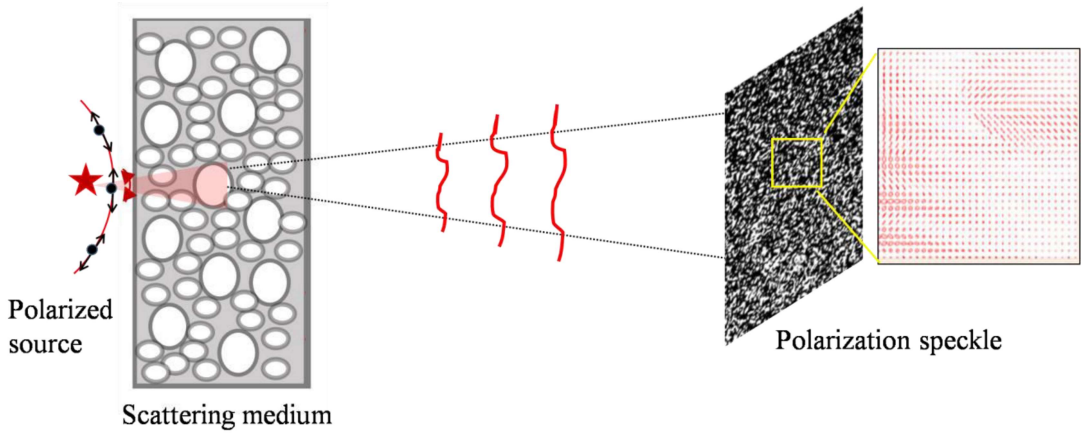

Fig. 1.25 Sketch for generation of polarization speckle. Polarization state distribution in part of the speckle is highlighted on the right-hand side.

Here, SPs illustrate the state of polarization (SOP) at a point, and the SOP is geometrically visualized on a Poincare sphere (Goldstein, 2017) as shown in Fig.1.26 (b). Fig. 1.26 (a) represents one snapshot of fluctuating random light field at a particular time t. Statistical characterization of the random electromagnetic fields demands consideration of coherence and polarization together. The joint effect of coherence and polarization plays an important role in the characterization of fluctuating electromagnetic fields (Gori, 1998; Wolf, 2007), and great efforts have been made to unify the coherence polarization in a common framework (Wolf, 2007). The correlation of fields at two different points, be it time or space, determines the coherence property of light. Two-point correlations of the electric field components in the vectorial regime are a matter of considerable interest. The electromagnetic degree of coherence that incorporates the correlation of all field components has also been proposed; it has information on both fringe visibility and polarization characteristics (Tervo, 2003). In the next section, the correlations at the two points are extended to deal with electromagnetic fields and the coherence-polarization matrix is discussed (Wolf, 2007, Gori, 1998).

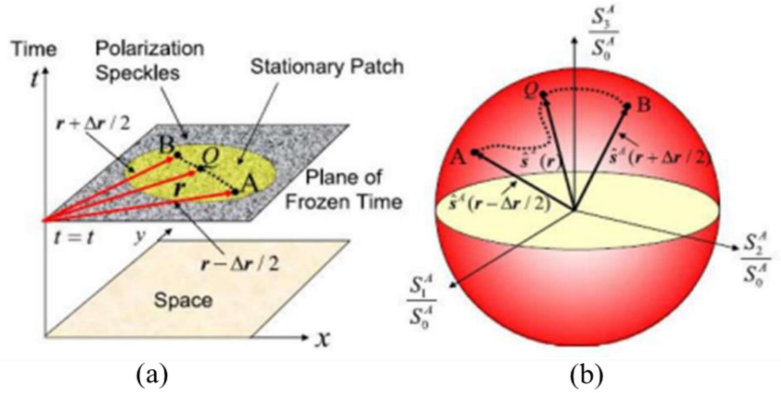

Fig. 1.26 (a) Snapshot of the fluctuating random field**, (b)** dynamics of polarization change in a single random pattern (at a frozen time t) is represented at the Poincare sphere. The SOPs in the random field is varying from point A to B. (Singh, 2014).

1.9.3.4 Coherence polarization matrix

A coherence polarization matrix is a significant tool to characterize the spatial coherence and polarization features of randomly fluctuating polarized light (Gori, 1998; Wolf, 2007). The diagonal elements of the matrix possess the coherence properties of the random light of a random electromagnetic field while off-diagonal elements of this matrix are utilized to extract the vectorial features.

The statistical properties of the random polarized field are expressed by a 2-by-2 coherence polarization (CP) matrix (Wolf, 2007) as

$$W(r_1,r_2)=\begin{bmatrix}\langle E_x^*(r_1)E_x(r_2)\rangle & \langle E_x^*(r_1)E_y(r_2)\rangle\\ \langle E_y^*(r_1)E_x(r_2)\rangle & \langle E_y^*(r_1)E_y(r_2)\rangle\end{bmatrix}$$

$$W(r_1,r_2)=\begin{bmatrix}\langle W_{xx}(r_1,r_2)\rangle & \langle W_{xy}(r_1,r_2)\rangle\\ \langle W_{yx}(r_1,r_2)\rangle & \langle W_{yy}(r_1,r_2)\rangle\end{bmatrix}, \tag{1.20}$$

where the angular bracket denotes the ensemble average. * is the complex conjugate, r_1 and r_2 are the two spatial points. The degree of coherence and polarization of the randomly

polarized light can be analyzed by the CP matrix. The degree of coherence of the stochastic electromagnetic field is represented (Wolf, 2007) as

$$\eta^2(r_1,r_2)=\frac{\sum_{jk}|W_{jk}(r_1,r_2)|^2}{\sum_{jk}W_{jj}(r_1,r_1)W_{kk}(r_1,r_1)},\quad \text{(j, k=x, y)}, \tag{1.21}$$

The degree of coherence is connected with the degree of polarization by the relation

$$P(r)=\sqrt{\eta^2(r)-1}, \tag{1.22}$$

$$P(r)=\sqrt{1-\frac{4\det W(r,r)}{|TrW(r,r)|^2}}, \tag{1.23}$$

where det stands for determinant and Tr is the trace. η and P represents the degree of coherence and polarization of the randomly polarized light respectively. The single-point correlation of the CP matrix is also referred to as the polarization matrix and is expressed as

$$J(r,r)=\begin{bmatrix}\langle E_x^*(r)E_x(r)\rangle & \langle E_x^*(r)E_y(r)\rangle\\ \langle E_y^*(r)E_x(r)\rangle & \langle E_y^*(r)E_y(r)\rangle\end{bmatrix}, \tag{1.24}$$

1.9.3.5 HBT for polarized light

With the development of a unified theory of coherence-polarization, electromagnetic (vector) fields have drawn significant attention (Perrin, 2012; Wolf, 2007; Sahin, 2009; Xin, 2008; Alonso, 2006; Kuebel, 2009; Tervo, 2003). Tervo el. al. discussed the intensity correlation for vector fields in the space-time domain and showed that the electromagnetic degree of coherence can be determined by the intensity correlation and this relation is explained in terms of contributions of all four components of the

coherence-polarization matrix for the field obeying Gaussian statistics (Tervo, 2003). The extension of the intensity correlation to the vector field is briefly explained here.

Let us consider a stochastic polarized light field that propagates along the z direction to the two detectors as shown in Fig. 1.27.

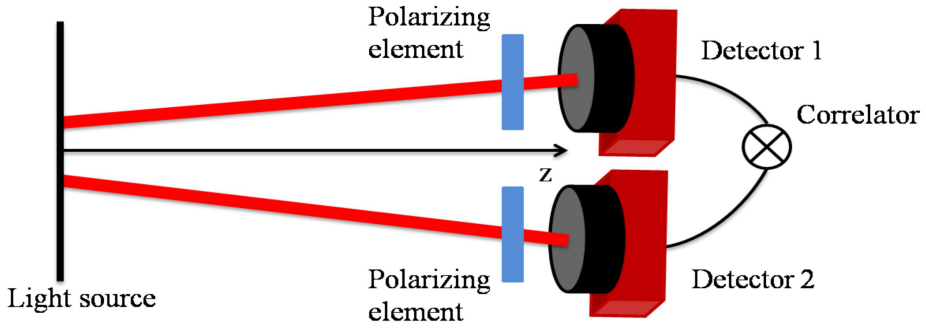

Fig. 1.27 Schematic diagram of intensity correlation of vector field.

The electromagnetic degree of coherence of the vector light is given as

$$\eta^2(r_1, r_2) = \frac{tr[W(r_1, r_2)W(r_2, r_1)]}{\langle I(r_1)\rangle\langle I(r_2)\rangle} \tag{1.25}$$

Fluctuations of the intensities from its mean value are given as

$$\langle \Delta I(r)\rangle = I(r) - \langle I(r)\rangle \tag{1.26}$$

Under consideration of the Gaussian random process and applying the Siegert relation, the correlation of the cross-covariance at two points is given as

$$\langle \Delta I(r_1)\Delta I(r_2)\rangle = \sum_{m,n} \left|W_{mn}(r_1, r_2)\right|^2 = tr[W(r_1, r_2)W(r_2, r_1)] \tag{1.27}$$

The degree of coherence of the stochastic electromagnetic beam can also be expressed as a second-order intensity correlation as follows

$$\eta^2(r_1, r_2) = \frac{\langle \Delta I(r_1) \Delta I(r_2) \rangle}{\langle I(r_1) \rangle \langle I(r_2) \rangle}. \quad (1.28)$$

The normalized correlation of intensity fluctuations is equal to the square of the degree of coherence for electromagnetic fields. The inclusion of polarization with intensity correlation has been demonstrated to design stable imaging systems for the reconstruction of the complete wavefront of the light from randomness (Singh, 2018; Vinu, 2016).

1.9.3.6 Polarization correlation

The correlation between the SPs at two points is referred to as the polarization correlation (Kuebel, 2019; Wang, 2019).

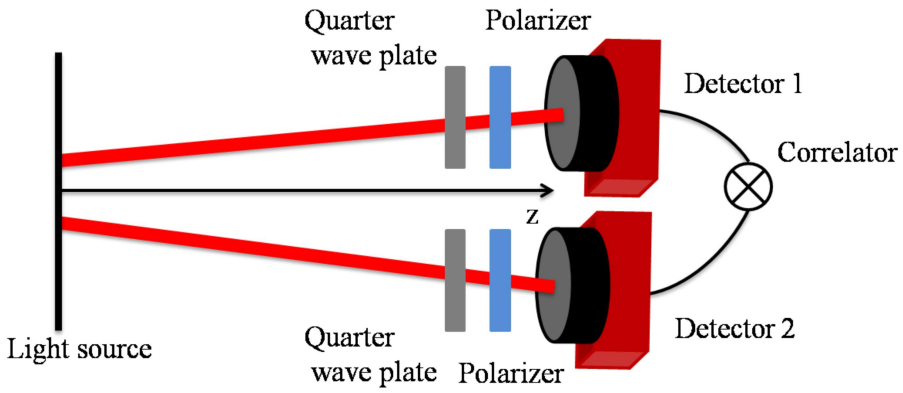

Fig. 1.28 Schematic diagram for the polarization-resolved HBT experiment.

A schematic diagram for the polarization correlation is shown in Fig. 1.28. The field that is incident on the two detectors is passed through polarizing elements (quarter wave plate, polarizer, etc.) to measure polarization states of the light field. The polarization states of the electromagnetic field are analyzed by four Stokes parameters (SPs) which are defined at position r as

$$
\begin{aligned}
S_0(r) &= E_x^*(r)E_x(r) + E_y^*(r)E_y(r),\\
S_1(r) &= E_x^*(r)E_x(r) - E_y^*(r)E_y(r),\\
S_2(r) &= E_x^*(r)E_y(r) + E_y^*(r)E_x(r),\\
S_3(r) &= i\left[E_y^*(r)E_x(r) - E_x^*(r)E_y(r),\right],
\end{aligned}
\tag{1.29}
$$

A fluctuation in the SPs is represented as

$$\Delta S_p(r) = S_p(r) - \left\langle S_p(r)\right\rangle, \text{ (p=0,..,3)}, \tag{1.30}$$

where S_p indicates a single realization of the stochastic field and $\left\langle S_p(r)\right\rangle$ is the ensemble average. All possible pairs of their two-point correlation are evaluated by a 4x4 stokes fluctuations correlation matrix as

$$C_{pq}(r_1, r_2) = \left\langle \Delta S_p(r_1)\Delta S_q(r_2)\right\rangle, \quad \text{(p, q=0,..,3)}, \tag{1.31}$$

Under the consideration of Gaussian statistics, the elements of the matrix are expressed as

$$C_{pq}(r_1, r_2) = \sum_{a,b}\sum_{c,d}\sigma_{ab}^p\sigma_{cd}^q W_{ad}(r_1, r_2)W_{bc}^*(r_1, r_2). \quad \text{(a, b, c, d=x, y)}, \tag{1.32}$$

where σ denotes the Pauli spin matrices and is represented as

$$\sigma^0 = \begin{pmatrix} 1 & 0 \\ 0 & 1 \end{pmatrix}, \sigma^1 = \begin{pmatrix} 1 & 0 \\ 0 & -1 \end{pmatrix}, \sigma^2 = \begin{pmatrix} 0 & 1 \\ 1 & 0 \end{pmatrix}, \sigma^3 = \begin{pmatrix} 0 & -i \\ i & 0 \end{pmatrix}, \tag{1.33}$$

All the sixteen elements of the matrix from Eq. (1.32) are represented as

$$C_{pq}(r_1, r_2) = \begin{pmatrix} C_{00}(r_1, r_2) & C_{01}(r_1, r_2) & C_{02}(r_1, r_2) & C_{03}(r_1, r_2) \\ C_{10}(r_1, r_2) & C_{11}(r_1, r_2) & C_{12}(r_1, r_2) & C_{13}(r_1, r_2) \\ C_{20}(r_1, r_2) & C_{21}(r_1, r_2) & C_{22}(r_1, r_2) & C_{23}(r_1, r_2) \\ C_{30}(r_1, r_2) & C_{31}(r_1, r_2) & C_{32}(r_1, r_2) & C_{33}(r_1, r_2) \end{pmatrix}, \tag{1.34}$$

For example, the element $C_{00}(r_1, r_2)$ is computed as

$$C_{00}(r_1,r_2)=\sum_{a,b}\sum_{c,d}\sigma^0_{ab}\sigma^0_{cd}W_{ad}(r_1,r_2)W^*_{bc}(r_1,r_2),$$

$$=\sigma^0_{xx}\sigma^0_{xx}W_{xx}(r_1,r_2)W^*_{xx}(r_1,r_2)+\sigma^0_{xx}\sigma^0_{yy}W_{xy}(r_1,r_2)W^*_{xy}(r_1,r_2)+$$

$$\sigma^0_{yy}\sigma^0_{xx}W_{yx}(r_1,r_2)W^*_{yx}(r_1,r_2)+\sigma^0_{yy}\sigma^0_{yy}W_{yy}(r_1,r_2)W^*_{yy}(r_1,r_2),$$

$$=\left|W_{xx}(r_1,r_2)\right|^2+\left|W_{xy}(r_1,r_2)\right|^2+\left|W_{yx}(r_1,r_2)\right|^2+\left|W_{yy}(r_1,r_2)\right|^2. \quad (1.35)$$

Similarly, working out Eq. (1.32) all sixteen elements are evaluated as

$$C_{01}(r_1,r_2)=|W_{xx}(r_1,r_2)|^2-|W_{xy}(r_1,r_2)|^2+|W_{yx}(r_1,r_2)|^2-|W_{yy}(r_1,r_2)|^2, \quad (1.36)$$

$$C_{02}(r_1,r_2)=2\,\mathrm{Re}\left[W_{xx}(r_1,r_2)W^*_{xy}(r_1,r_2)+W_{yy}(r_1,r_2)W^*_{yx}(r_1,r_2)\right], \quad (1.37)$$

$$C_{03}(r_1,r_2)=2Im\left[W_{yy}(r_1,r_2)W^*_{yx}(r_1,r_2)-W_{xx}(r_1,r_2)W^*_{xy}(r_1,r_2)\right], \quad (1.38)$$

$$C_{10}(r_1,r_2)=|W_{xx}(r_1,r_2)|^2+|W_{xy}(r_1,r_2)|^2-|W_{yx}(r_1,r_2)|^2-|W_{yy}(r_1,r_2)|^2, \quad (1.39)$$

$$C_{11}(r_1,r_2)=|W_{xx}(r_1,r_2)|^2-|W_{xy}(r_1,r_2)|^2-|W_{yx}(r_1,r_2)|^2+|W_{yy}(r_1,r_2)|^2, \quad (1.40)$$

$$C_{12}(r_1,r_2)=2\,\mathrm{Re}\left[W_{xx}(r_1,r_2)W^*_{xy}(r_1,r_2)-W_{yy}(r_1,r_2)W^*_{yx}(r_1,r_2)\right], \quad (1.41)$$

$$C_{13}(r_1,r_2)=2Im\left[W_{xy}(r_1,r_2)W^*_{xx}(r_1,r_2)+W_{yx}(r_1,r_2)W^*_{yy}(r_1,r_2)\right], \quad (1.42)$$

$$C_{20}(r_1,r_2)=2\,\mathrm{Re}\left[W_{xx}(r_1,r_2)W^*_{yx}(r_1,r_2)+W_{yy}(r_1,r_2)W^*_{xy}(r_1,r_2)\right], \quad (1.43)$$

$$C_{21}(r_1,r_2)=2\,\mathrm{Re}\left[W_{xx}(r_1,r_2)W^*_{yx}(r_1,r_2)-W_{yy}(r_1,r_2)W^*_{xy}(r_1,r_2)\right], \quad (1.44)$$

$$C_{22}(r_1,r_2)=2\,\mathrm{Re}\left[W_{xx}(r_1,r_2)W^*_{yy}(r_1,r_2)+W_{xy}(r_1,r_2)W^*_{yx}(r_1,r_2)\right], \quad (1.45)$$

$$C_{23}(r_1,r_2)=2Im\left[W_{xy}(r_1,r_2)W^*_{yx}(r_1,r_2)+W_{yy}(r_1,r_2)W^*_{xx}(r_1,r_2)\right], \quad (1.46)$$

$$C_{30}(r_1,r_2)=2Im\left[W_{xx}(r_1,r_2)W^*_{yx}(r_1,r_2)-W_{yy}(r_1,r_2)W^*_{xy}(r_1,r_2)\right], \quad (1.47)$$

$$C_{31}(r_1,r_2)=2Im\left[W_{xx}(r_1,r_2)W^*_{yx}(r_1,r_2)+W_{yy}(r_1,r_2)W^*_{xy}(r_1,r_2)\right], \quad (1.48)$$

$$C_{32}(r_1,r_2)=2\,\mathrm{Im}\left[W_{xy}(r_1,r_2)W_{yx}^{*}(r_1,r_2)+W_{xx}(r_1,r_2)W_{yy}^{*}(r_1,r_2)\right], \tag{1.49}$$

$$C_{33}(r_1,r_2)=2\,\mathrm{Re}\left[W_{xx}(r_1,r_2)W_{yy}^{*}(r_1,r_2)-W_{xy}(r_1,r_2)W_{yx}^{*}(r_1,r_2)\right], \tag{1.50}$$

The different combinations of the elements of the polarization-correlation matrix can be used for phase recovery and polarization correlation holography methods etc. Details of some of these techniques will be discussed in the upcoming chapters.

1.10. Delivery and recovery of 3D optical information with coherence holography

The correlation features of the random light are exploited in the development of a remarkable unconventional holography technique for the delivery and recovery of 3D optical information with random light. This unconventional holography approach, named coherence holography, uses a two-point complex correlation function to reconstruct the complex and 3D object information (Takeda, 2005, 2021). The technique employs the formal analogy between the formula of the van-Cittert Zernike theorem and the diffraction integral, where the correlation function follows the same wave equation as the optical field (Takeda, 2021). The basic principle of the CH is explained as follows:

The principle of coherence holography is based on the similarity between the coherence function $W(r_1,r_2,t_1,t_2)$ and the optical field $E(r,t)$ as both follow the wave equation.

(Coherence function) (Optical field)

$$\nabla^2_{i=1,2}W(r_1,r_2,t_1,t_2)=\frac{1}{c^2}\frac{\partial^2 W(r_1,r_2,t_1,t_2)}{\partial t^2_{i=1,2}}, \qquad \nabla^2 E(r,t)=\frac{1}{c^2}\frac{\partial^2 E(r,t)}{\partial t^2}, \tag{1.51}$$

As a consequence of this analogy, a similarity is also found between the diffraction integral and the van-Cittert Zernike theorem. For instance, a Fourier hologram shown in Fig. 1.29 (a) is reconstructed in terms of the optical field. On the other hand, illumination

of the Fourier hologram by random light reconstructs the hologram as a spatial distribution of the spatial coherence as shown in Fig. 1.29 (b). This idea has been used to design and develop various correlation-based imaging and coherence synthesis techniques (Naik, 2012, Singh, R., 2014; Vinu, 2016; Chen, 2020). Moreover, the inclusion of polarization in the coherence holography helps to develop and design techniques such as vectorial coherence holography (Singh, R., 2011) and Stokes holography (Singh, R., 2012) for recovery of the complete wavefront.

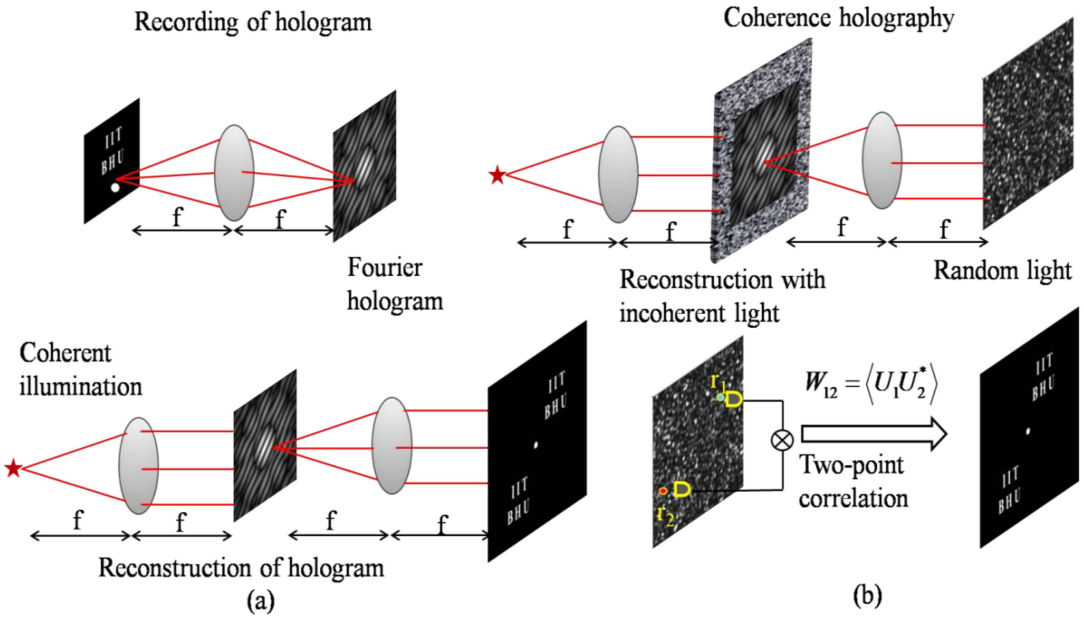

Fig. 1.29 (a) Reconstruction in conventional holography with coherent illumination, **(b)** reconstruction in coherence holography with random light.

The challenge of phase recovery in the intensity correlation has been addressed by developing a speckle holography technique in combination with a two-point intensity correlation (Singh, R., 2014). In this technique, the off-axis holography was combined with intensity correlation to recover complex coherence function and consequently the complex field. Further, the concept is extended to design several non-invasive imaging techniques for the complex field recovery of objects obscured by the scattering media

(Somkuwar, 2017; Vinu, 2019; Chen, 2020, 2021, 2022). Recently, the off-axis holography with intensity correlation was utilized to evaluate the correlation between two orthogonal polarization components, and this helped to recover the complex amplitude of the helical beam [Vinu, 2016].

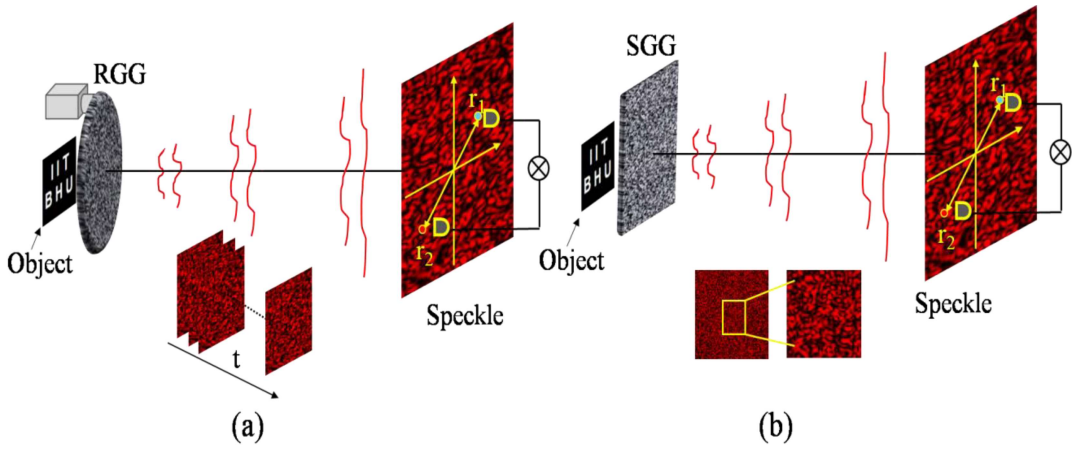

Fig. 1.30 (a), (b) Denote schematic for temporal and spatial averaging operations respectively. RGG: rotating ground glass, SGG: static ground glass.

This recent progress in coherence holography techniques show applications in imaging with single speckle pattern based on spatial statistical optics rather than temporal statistics (Naik, 2012; Takeda, 2014). Moreover, the concept of spatial statistical optics and spatial averaging helps in analyzing spatially fluctuating random fields. To illustrate an idea about spatial averaging, the ensemble average, a mathematical basis of statistical optics, is commonly supplanted with time averaging under the assumption that the statistical field is stationary and ergodic in time (Takeda, 2013, 2014) as applied in Fig. 1.30 (a). However, the time average method for reconstruction is computationally cumbersome due to the requirement of a huge number of random patterns. On the other hand, spatial averaging provides a single-shot reconstruction method from a single random pattern under the consideration of the statistical field being stationary and ergodic in space (Takeda, 2013, 2014) as shown in Fig. 1.30 (b). In this thesis, we mainly concentrate on

an analysis of the speckle field using polarization correlations for the recovery of optical information from the speckle patterns using spatial statistical optics.